Energy 147 (2018) 547–560

Contents lists available at ScienceDirect

Energy

journal homepage: www.elsevier.com/locate/energy

# Conceptual design and performance evaluation of a hybrid concentrating photovoltaic system in preparation for energy

Hasan Baig [a], J. Siviter [b], W. Li [b], M.C. Paul [b], A. Montecucco [b], M.H. Rolley [c], T.K.N. Sweet [c], M. Gao [c], P.A. Mullen [b], E.F. Fernandez [d], G. Han [e], D.H. Gregory [e], A.R. Knox [b], Tapas Mallick [a, *]

[a] Environmental and Sustainability Institute, University of Exeter, Penryn, UK
[b] School of Engineering, University of Glasgow, Glasgow, UK
[c] Cardiff School of Engineering, Cardiff University, Cardiff, UK
[d] Centre for Advanced Studies in Energy and Environment, University of Jaen, Jaen, Spain
[e] WestCHEM, School of Chemistry, University of Glasgow, Glasgow, UK

ARTICLE INFO

*Article history:*
Received 10 August 2017
Received in revised form
7 December 2017
Accepted 24 December 2017
Available online 28 December 2017

*Keywords:*
LCPV/T
CPC
CCPC
Hybrid

ABSTRACT

Concentrating sunlight and focussing it on smaller sized solar cells increases the device's power output per unit active area. However, this process tends to increase the solar cell temperature considerably and has the potential to compromise system reliability. Adding a heat exchanger system to regulate this temperature rise, can improve the electrical performance whilst simultaneously providing an additional source of low temperature heat. In this study the performance of a low concentrator photovoltaic system with thermal (LCPV/T) extraction was conceptualised and evaluated in depth. An experimental analysis was performed using a first-generation prototype consisting of 5 units of Cross Compound Parabolic Concentrators (CCPC) connected to a heat extraction unit. A bespoke rotating table was used as experimental apparatus to effectively evaluate the optical performance of the system, as a function of its angular positions to replicate the motion of actual sun. Key design performance parameters for the LCPV/T collector are presented and discussed. This work also provides a useful technique to effectively calculate system performance, as a function of the orientation-dependant electrical characterisation parameters data. Finally, a Computational Fluid Dynamics (CFD) model was also applied to investigate the efficacy of the heat exchanger and hence estimate the overall co-generation benefit of using such optimisation techniques on realistic CPV systems. It was highlighted through these simulations that the water flow rate had the potential to be a critical power-generation optimisation criterion for LCPV-T systems. The maximum power output at normal incidence with concentrators and no water flow was found to be 78.4 mW. The system was found to perform with an average electrical efficiency ranging between 10 and 16% when evaluated at five different geographic locations. Experimental analysis of the data obtained showed an increase in power of 141% (power ratio 2.41) compared to the analogous non-concentrating counterpart. For example, in the case of London which receives an annual solar radiation of 1300 kWh/m$^2$ the system is expected to generate 210 kWh/m$^2$. This may reduce further to include losses due to temperature, reflectance/glazing losses, and electrical losses in cabling and inverter by up to 36% leading to an annual power output of 134 kWh/m$^2$ of module.



## 1. Introduction

Photovoltaics (PV) cells are manufactured from semi-conductors that inherently in their deployment operate on a logical paradox – they need sunlight to generate electricity but suffer a degradation in performance as they get hotter. Hybrid Photovoltaic-Thermal (PV/T) technologies combine a photovoltaic cell, which converts electromagnetic radiation (photons) into electricity, with a solar thermal collector that captures the remaining energy and removes waste heat from the PV module.

* Corresponding author.
*E-mail addresses:* h.baig@exeter.ac.uk, mail2baig@gmail.com (H. Baig), t.mallick@exeter.ac.uk (T. Mallick).

https://doi.org/10.1016/j.energy.2017.12.127

Such a system can provide both electrical and thermal energy at the same time whilst also reducing the area required to install two separate systems.

A further improvement to these systems can be made when combined with concentrated sunlight. The solar cell area can be effectively reduced without compromising on the obtained thermal output of system [1]. Low concentrator photovoltaic (LCPV) technologies (solar concentration <10) have been developed as research systems for the last three decades but are recently gaining interest for deployment at a commercial scale [2]. An addition of a thermal heat exchanger to this type of system, as investigated by this work, has the potential to be an effective way of maximizing the system solar energy generation potential in a cost-effective manner.

Typically, LCPV systems consist of a concentrator element coupled to a small sized solar cell. The incoming solar radiation gets focused on the small sized solar cell hence increasing the electrical output from the solar cell. However, this increased light intensity can drop the performance of typical screen printed Si solar cells, which is why special Laser Grooved Buried Contact (LGBC) solar cells are more appropriate for such applications [3]. These Si solar cells are designed to operate under higher solar concentration (up to 100 × ) [4]. Non-imaging optics are adopted to achieve solar concentration, as an optical image is not necessary as long as the concentration increase is conserved. This is achieved through total internal reflection within the optic design. These optics do not require precision manufacturing as required for imaging optics, and as such can be easily manufactured using cheap materials. Both refractive and reflective optical elements have been developed for optical concentration. Reflective type concentrators offer a comparatively high optical efficiency, whereas the refractive type systems typically offer better acceptance angles for LCPV systems. Among non-imaging optics the Compound Parabolic Concentrator (CPC) is one of the most popular designs [5–10], a representative of which is shown in Fig. 1. The CPC geometry was initially developed by Winston [11,12], and has since been further examined by several others [4,13]. A Compound Parabolic Concentrator (CPC) for solar energy applications, consists of two different parabolic reflectors which in addition to the direct solar radiation absorbed directly by the absorber can reflect both the direct and some diffuse incident radiation received at the absorber entrance aperture. The geometry of the CPC can be formed by rotating the axis of a given lens parabola through the acceptance angle. The acceptance angle defines the maximum limit for the incident light to be focused or collected by the concentrator. Further improvements to the CPC shape have been made with asymmetric concentrating photovoltaic systems [14,15] which utilise parabolic profiles rotated at different angles followed by truncation.

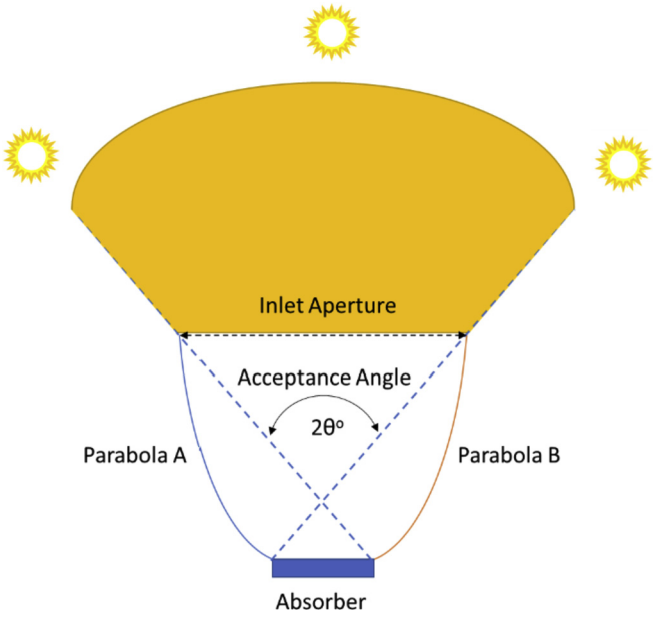


**Fig. 1.** Schematic diagram of a Compound parabolic concentrator (CPC).

Several designs of 3D concentrators have been proposed for CPV applications based on CPC geometry. The 3D concentrator principally concentrates light from all the directions, unlike a linear concentrator. One of the first designs proposed for the building integration of LCPV is the reflective 3D crossed compound parabolic concentrator (3DCCPC) [16]. This system consisted of an array of 3DCCPC placed over 1 $cm^2$ sized LGBC PV cells. The developed system achieved optical efficiencies of 75% experimentally even with a substantial 60° acceptance angle (2θ). Following on from this, an improved optical efficiency of 81% was achieved experimentally in the second prototype of the system highlighting the potential of such a LCPV lens geometry. Based on a similar design a refractive-based 3DCCPC was modelled and experimentally evaluated [6]. The refractive-based system had a higher acceptance angle as compared to the reflective type system. Detailed optical, electrical, and thermal modelling of the system was carried out and experimentally validated. A maximum power ratio of 2.67 with an acceptance angle of 80° was found when comparing the electrical output of the concentrator unit with the bare cell. Additionally, the temperature was found to have a substantial parasitic effect on the overall performance of the system with an observed 14.6% drop in overall power production. A further enhancement to the above system was reported recently, where light trapping was performed by applying a reflective film along the edges of the 3DCCPC concentrator. This technique gave an improved maximum power ratio of 2.73. The system optical efficiency was improved with the trade-off of a slightly reduced acceptance angle.

Several new concepts of CPV systems have been demonstrated recently [17–20] with an increasing number deploying 2D CPC designs as the concentrating element. Results have shown that these systems can generate much greater electrical power when compared with a non-concentrating system. Li. et al. [18] performed a detailed numerical and experimental analysis of an air-gap-lens-walled compound parabolic concentrator (2.4×) incorporated within photovoltaic/thermal system (ALCPC-PV/T). The system however was found to have very low electrical efficiency of 6% and a thermal efficiency of 35%. Haitham et al. experimentally [19] evaluated the increase in efficiency possible through the cooling of a flat plate panel and a PV panel with concentrators [21] under the hot climate of Saudi Arabia. Mahmoud et al. used GaAs solar cells [17] in a novel double-stage high-concentrated solar hybrid photovoltaic/thermal which used concentrating parabolic reflectors. The maximum total system electricity generation achieved by the system was estimated to be around 25% of the incoming DNI. This design achieved an effective ~60 × concentration from the parabolic aperture, which is significantly higher than many conventional CPV/T systems.

In the present study, we highlight an improved design for a Concentrating Photovoltaic Thermal, system based on the well-respected reflective 3DCCPC. The key novelty of this system is that it directly bonded the silicon solar cells onto a conductive heat exchanger using a thermal conductive medium. An optical analysis of the system was carried out using ray tracing techniques and its indoor performance experimentally evaluated. The thermal performance of the system was also studied.

## 2. System design & manufacture

### 2.1. System components

(a) Optics

The optical design used in the system was based around the well-established reflective 3D Crossed Compound Parabolic Concentrator (3DCCPC). The profile of a CPC was swept around a square to generate the used 3DCCPC profile [6]. The optical acceptance of this geometry was calculated to be ±30°. The optical acceptance of the geometry is designed to achieve useful concentration without tracking. The acceptance range helps in concentrating most of the direct sunlight within which occur during the ±2 h of the solar noon. Previously [16] similar geometry was used in a building integrated concentrating photovoltaic system to maximise the energy yield. The optic was designed to have an exit aperture of 1 $cm^2$ and had a truncated height of 15.8 mm with an entrance aperture sized 3.6 times larger than the exit aperture. One key benefit of such a design criterion is that it permits a significant collection of sunlight throughout the day. Another benefit, was that in comparison to other high concentration systems which require very expensive optics, these type of optics can be manufactured very cheaply. A groove was made along the base of the concentrator for creating a robust electrical connection between the adjacent solar cells within a string as shown in Fig. 2. This groove also helped in maintaining the vertical alignment of the solar cells, a factor crucial for facilitating effective optical coupling. Ray tracing is a standard technique for evaluation of the optical performance of concentrators. A given number of rays can be traced to represent the solar radiation incident on a concentrating system. In this present study, all incident rays were assumed to be parallel and carry an equal amount of energy. These incident rays are reflected by the parabolic profile and hence are concentrated on the solar cell surface as shown in Fig. 3.

Ray-trace simulations were carried out using the APEX® software package [22]. The optical properties of the reflective material used for making the 3DCCPC and the spectrum of the incoming solar radiation were kept in accordance with the experimental setup. The light distribution reaching the solar cell after concentration under normal incidence showed a non-uniformity [4] at the four corners of the solar cell. The impact of this was however found to be negligible on the overall performance of the system. For this design, the cell area was slightly bigger than the exit aperture of the optical unit to reduce any ohmic losses. Simulations show that the design exhibits a wide range of acceptance angles of ±30° as shown in Fig. 4. The maximum optical efficiency of the unit directly depends on the quality of the reflective surface used within the manufacture of the optic. In the present study, we utilised a reflective coating comparative to the reflectance achieved by thermal evaporative coatings which have an average reflectance of 96%. However, it is important to note that it is subject to the surface finish of the substrate.

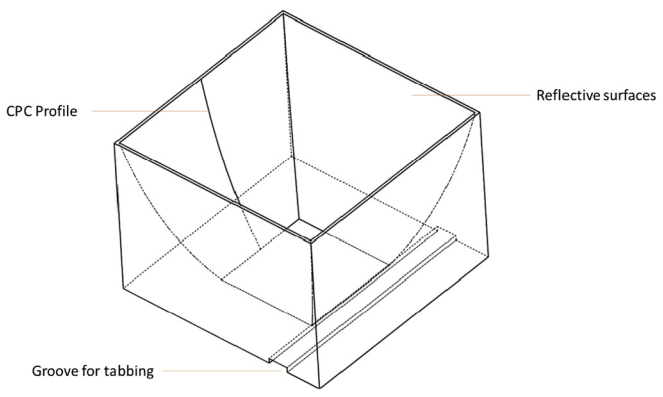


**Fig. 2.** A single unit of the concentrating optical element.

(b) PV Cell

The laser grooved buried contact (LGBC) process is an effective way to manufacture high efficiency solar cells using monocrystalline silicon. In this process, a laser is used to inscribe grooves into the silicon cell where fingers for the front contact are deposited by electro-plating technique which reduces the shading losses occurring due to the fingers. These cells are suitable for low to medium concentration systems due to this low contact shading [4]. Further details on the technique have been previously described in literature [23]. In general, smaller cells ensure a reduced material in addition to facilitating effective heat transfer in the system. In the present work, we have utilised solar cells having an active area of 1 $cm^2$ as shown in Fig. 5. The LGBC solar cells used in this system have been optimized to be used up to 50 × .

(c) Copper Tube heat sink

A (13mmx13 mm) square shaped copper tube was chosen for use as the heat exchanger. The tube had a 0.1 mm wall thickness with capped ends for ease of connection to the coolant network.

### 2.2. Prototype manufacturing

The optics as previously described, were fabricated using 3D printing with a Fused Deposition Modelling (FDM) technique. In this process, the CAD design of the component was imported into assisted software, wherein it is positioned in the 3D co-ordinate space relative to the 3D printer software datums. The design was then digitally “sliced” into layers, which hence described the movement path for the extruder head depositing the thermoplastic material. The process is a simple and an effective way of producing bespoke, high quality optical prototypes of complex geometries and curvatures. The printed prototype was then sanded to improve its surface finish. The plastic prototype was then coated with its reflective coating using thermal evaporation of aluminium. The reflective coating was further protected using a siloxane film deposited using plasma process as shown in Fig. 6.

The copper tube was cleaned prior to assembly to remove any oxidation layers that were present. The tube was marked as per the solar cell dimensions, leaving enough space to accommodate the solar concentrators. Along these marked locations, a thermal adhesive (PC 3001 Heraeus) was applied in limited and measured quantities. The silver-filled epoxy conductive adhesive is solvent free and of the thermosetting type, so requires oven curing at 200 °C. The key advantage of using this adhesive is that it has high electrical and thermal conductivity (>5 W/m. K). Any excess spillage of the adhesive along the edges of the solar cell can cause short-circuiting, emphasising the need of a careful manufacture process and appropriate considerations to be taken throughout the design stages. A summary of the complete assembly and manufacture method is shown in Fig. 7.

A quality-control check was performed to ensure there were no short-circuited solar cells after bonding. A k-type insulation was placed between the solar cells to ensure they were adequately located as is crucial for effective optical coupling to the cell active area. Further the solar cells were hand-soldered to connect the bus bars in parallel. The copper tube acted as a rear-side common

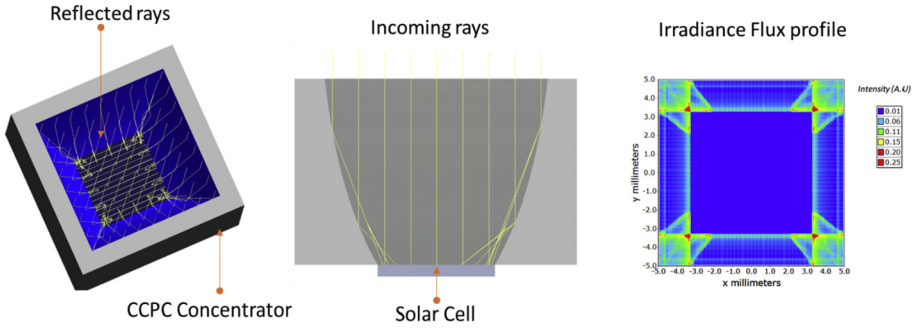


**Fig. 3.** Ray tracing of the optical concentrator and irradiance flux profile on the solar cell.

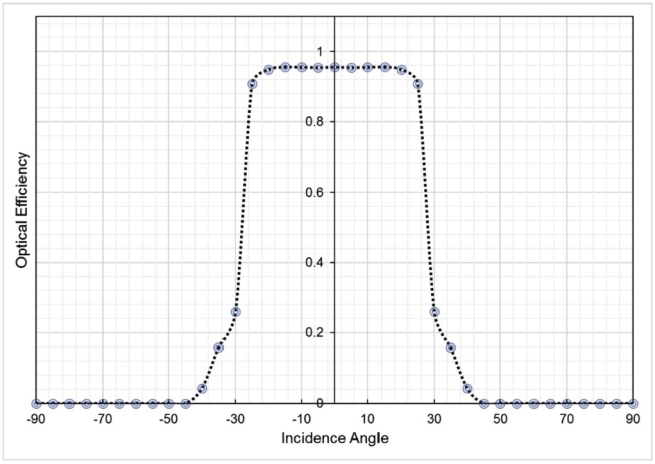


**Fig. 4.** Optical efficiency as a function of the incidence angle using ray tracing.

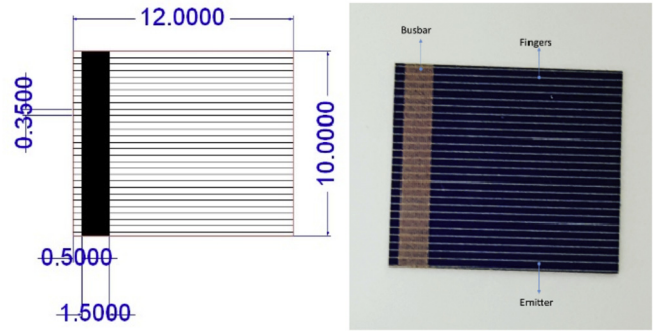


**Fig. 5.** LGBC solar cell used in the system.

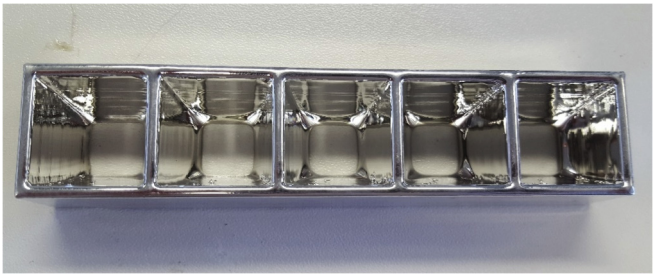

**Fig. 6.** Optics manufactured using 3d printing and evaporative coating.

terminal due to this method, streamlining the manufacture process. A voltage check was then carried out to ensure that all the solar cells were appropriately connected. Once this is done the 3-d printed optical concentrator was attached on the top of the solar cell to complete the assembly of the unit using a thin layer of Sylguard encapsulant. This encapsulation layer protected the solar cell against any environmental damage and hence improved device robustness.

## 3. Experimental tests and multiphysics simulation

This section provides details of the indoor experimental characterisation of the concentrator unit evaluating its optical, electrical, and thermal performances. The IV characterisation of the system is reported based on the angular and intensity variations of the incoming irradiance. The performance of the system under the solar simulator was compared with a non-concentrating counterpart to evaluate the effective optical efficiencies.

### 3.1. Rotating table

Typically, the testing of PV cells is carried out using standard illumination conditions of AM1.5G at 1000 W/m$^2$ and a temperature of 25 °C. However, this limits our understanding when evaluating solar concentrator systems. Previously [24], a manually operating inclination table was used to evaluate the performance of the concentrating photovoltaic system. However, this limits the angular performance variation in only one direction and is more suitable for the linear solar concentrators. The incoming solar radiation is predominantly a function of the geographical location, day, and the time of the year. To simulate the performance of this system a customised system was developed that can virtually simulate the sun intensity levels at any point on the earth and at any time or over a period. The system in theory allows for the accurate positioning of a PV cell array having an area of 25 × 25 cm directly beneath a collimated light solar source while altering azimuth and elevation – as relating to the geographical position and time required. By applying previously developed solar time and location calculations and algorithms, it was possible to develop a test system that could position the PV cell underneath a solar source to simulate any solar illumination on the earth. The algorithm selected for this test system was based on [25] to take the date, time and desired location on the earth, and then convert this to the solar azimuth and elevation. The work has been expanded to include the elevation however for the purposes of evaluation of the test system this has been excluded and assumed to be sea level. This algorithm was then converted into a MATLAB script and interfaced into a test program Graphical User Interface (GUI).

The test system consisted of five axes of movement: x, y, rotation, azimuth, and elevation. The solar azimuth and elevation were

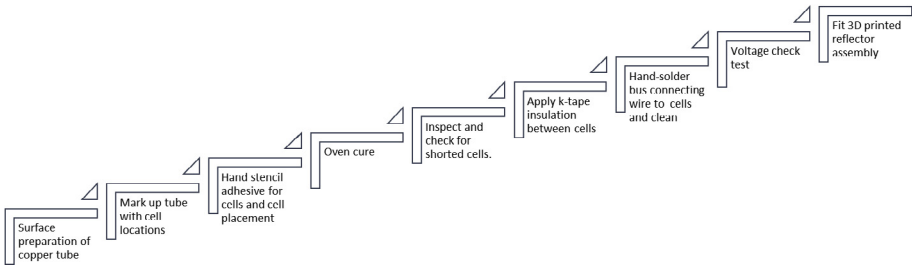


**Fig. 7.** Processes in the prototype manufacture.

translated to the test system to account for the difference in zenith and azimuth as shown in Fig. 8. A schematic showing these angles is presented in Fig. 9. The test system operated by the movement of various platforms controlled by stepper motors. The azimuth and elevation were actuated upon set gear ratios that allow for a time accuracy of 10 s over a 24 h period. The test system independently actuated five stepper motors, three scaled to the gear ratios of the azimuth and elevation axes and two for the x and y positioning. Each stepper motor was individually controlled to allow for simultaneous movement, hence allowing for quick and near-real time positioning. The test system was built on an Arduino platform consisting of five stepper motor driver controllers and a serial interface to communicate to a MATLAB based platform. The azimuth and elevation controls were calculated independently and then translated to several steps to pulse the stepper motor. Through appropriate optimisation of the software code, the MATLAB interface effectively queued a series for instructions to the test system, allowing for the continuous operation of all axes simultaneously without an additional processing delay. The test system comprising the movement of x, y, rotation, azimuth, and elevation axes 'reset' to allow for accurate positioning from when the system calculates and moves to a desired position. The 'reset' functionality was achieved using limit detection on the x and y axes, and gyroscopic accelerometer readings for the elevation and azimuth axes. The 3-axis gyroscope is based on the Mems Sensor L3G4200D [26], reporting the roll (θ-axis), pitch (ω -axis) and yaw (ψ -axis) of the solar tracker table as shown in Fig. 10 for use within the Arduino algorithm.

To ensure the accurate positioning of the elevation axis, the angle of the platform was compared automatically, as a feedback loop to the motor driver controller, with both the number of steps the axis moves by and the resultant measured gyroscope angle. Hence any geometrical positioning errors were compensated for by adjusting the respective stepper motor axis to this corrective gyroscope reading.

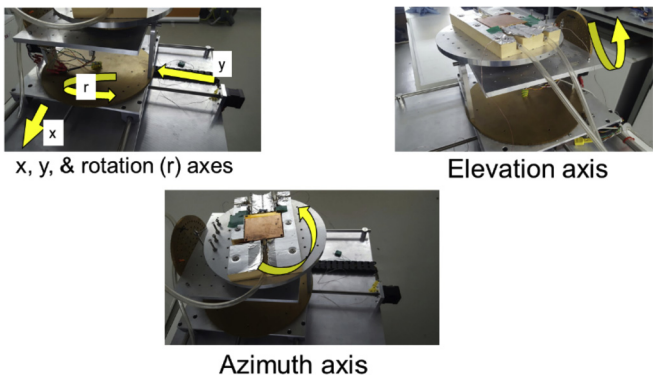


**Fig. 8.** Test system showing each of the axes.

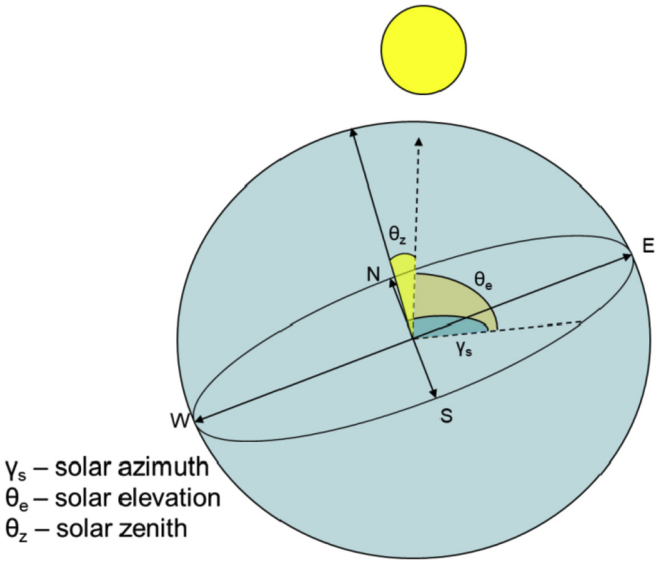


**Fig. 9.** Depiction of solar zenith, solar elevation and solar azimuth.

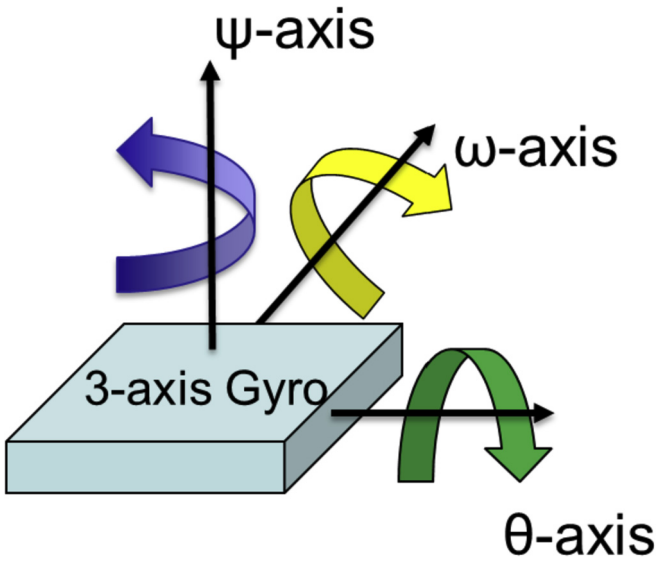


**Fig. 10.** 3-Axis Gyroscope based on L3G4200D.

The testing methodology used, placed the PV cell on the horizontal plane and then measured the I-V characteristics at a given constant irradiance. To simulate the movement of the sun over the course of the day, the platform repositioned for each successive point in time. The desired date, geographical coordinates and time

steps were input into the MATLAB GUI and the resultant azimuth and elevation data outputted to the motors to effectively plot the course of the sun over the defined time intervals. As part of the testing for this work the solar tracker was set to calculate the incremental number of steps from the present position rather than perform a 'reset' operation each time.

The source for the solar radiation (Class AAA Wacom Solar Simulator, collimation angle 1.43) was also interfaced to the MATLAB program, allowing the source radiation is read in as a variable and likewise a parameter that could be adjusted automatically depending on the experimentally desired irradiation (Fig. 11). The only limitation of the setup is that we cannot control the change in spectrum while changing the angle and the light intensity. This may lead to some mismatch with theoretical predictions due to the wavelength dependence of each of the materials used.

### 3.2. Experimental setup

Detailed parameters can be extracted from the I–V characteristics of a solar cell, and as such this technique is considered as the best method to evaluate the cell electrical performance. A special setup with the rotating table as shown in Fig. 12, was used to change the angular position of the concentrator unit designed in this work. A "AAA" class WACOM solar simulator was used as the source of collimated light [27] at a standard irradiation of 1000 W/$m^2$ and AM1.5G spectrum and can be modulated as required.

The IV-curve measurement of the devices was carried out using an IV curve tracer (EKO Model no MP160). The IV tracer had a maximum rated power measurement for PV devices up to 300 W. This instrument can be used for both indoor characterisation of PV/CPV modules, using two different software packages. Important parameters such as, the maximum power point (MPP), fill factor (FF), open-circuit voltage (Voc), short circuit current (Isc), and short circuit current density (Jsc) can be extracted from the IV curve data obtained during the experiment. To start the experiment, the solar simulator was switched on for 1 h to warm up thereby establishing a steady energy flux output over the illumination area. The shutter was kept closed during this time. Once the solar simulator had warmed up, the light intensity at the working plane and area was measured using a calibrated solar cell. Both the non-concentrating (bare) and the concentrating devices were placed on the rotating table which was then tilted and rotated at angular intervals of 5° to record the I-V characteristics at each position. The IV-tracer used a 4-wire connection, 2 positive and 2 negative terminals to eliminate cable resistance errors during measurement. One pair of positive and negative connections were used to apply a biased voltage and the other pair were used to sense outputs from the module as

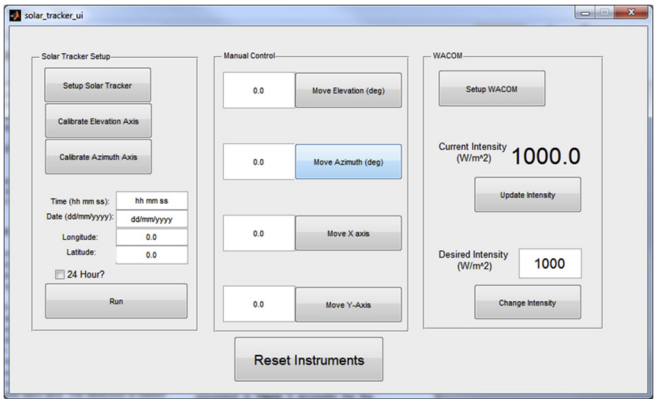


**Fig. 11.** Control and interface pogram in MATLAB

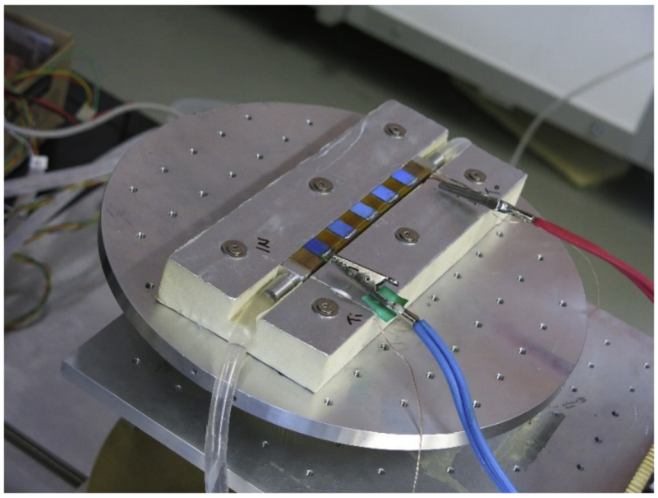

**Fig. 12.** Rotating table setup.

shown in Fig. 13. Thermal insulation was applied around the copper tube to prevent any heat losses from the copper tube and maintain a steady temperature of the device minimise the deviation from the adiabatic boundary conditions set in the thermodynamic modelling of the system, described later in this paper. Additionally, thermocouples were added at the inlet and the outlet of the copper tube to monitor the temperature of the cooling water.

### 3.3. Models and methods in multiphysics simulations

To carry out an effective optical analysis, the light source was switched on and off instantly to carry out the I-V measurements of the device. However, in realistic operation conditions, devices typically operate under transient conditions where the incoming water temperature and the amount of incoming solar radiation changes with the time of the day. To assess the steady state performance of the system an initial thermal performance analysis was carried out and linked with a numerical simulation as a basis to be further extended and predict the device performance in real time operation.

In this model, the cooling water was modelled to pass through the system over small intervals of time until a steady state was achieved under a fixed light intensity conditions. During these intervals, the temperature of the water entering and leaving the unit was measured with thermocouples as shown previously in Fig. 13. Since measuring the solar cell was difficult it was important to simulate the system using finite volume methods. A multiphysics simulation study was carried out to predict the cell temperature at a certain flow rate under cooling and no-cooling conditions. In the transient simulations, the measured ambient temperature and water temperature at the inlet of the heat exchanger were used as input conditions. The computational domain for the multiphysics simulations included five CCPC's and their respective PV cells, a 13 mm × 13 mm squared cross-sectional copper tube with 0.5 mm wall thickness, and a Sylguard layer as an optical coupling for the solar cells and the LCPV optics. The volume of fluid flow through in the tube and the five internal air bodies corresponding to the five cavities of CCPC, were also included as shown in Fig. 14.

Within the Multiphysics simulations, the material properties were appropriately selected to match with the experimental setup and are listed in Table 1. The multiphysics simulations were carried out using ANSYS CFX 15.0 in transient mode. In the air fluid domain, the 3D incompressible laminar flow model, natural convective heat

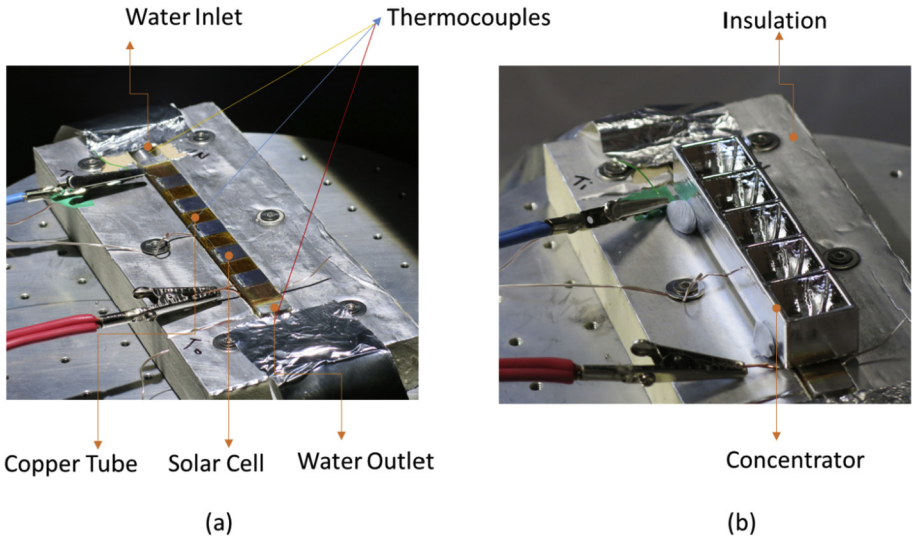


**Fig. 13.** Setup shows the system (a) without the concentrator (b) with the concentrator.

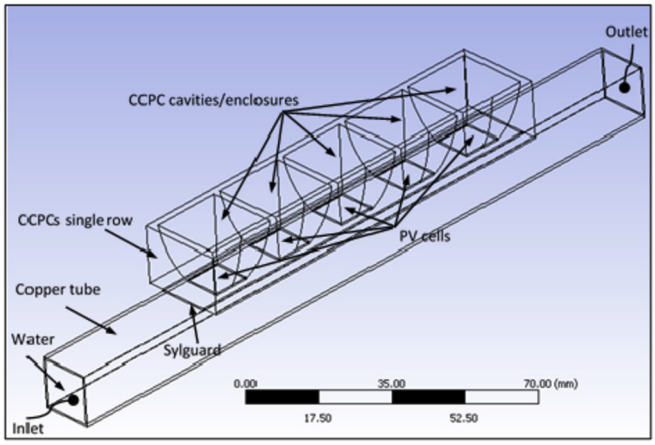


**Fig. 14.** Computational Domain of the system.

transfer and the radiation transportation equations were solved. The Bousinessq approximation was involved in the flow model by means of air expansion and the grey radiative implication was held consistent through the radiation model. In the CCPC and Sylguard layer solid domains, the conductive heat transfer and radiation transportation equations were used to improve the model accuracy. In the copper tube solid domain, the conductive heat transfer equations were selected, while for the fluid domain the forced convective heat transfer equations and 3D laminar incompressible flow models were implemented. Details of these equations can be found in the appendix.

Simulations were carried out using consistent atmospheric input conditions recorded from the experiment, of 1000 W/m$^2$ incoming solar irradiance and a water flow rate of 0.3lit/min. Both convective and radiative heat transfer effects were included in the simulation, a thermal emissivity 0.06 of aluminium was used on all the surfaces exposed to the ambient air for the CCPCs and Sylgard layer because the CCPCs are made of aluminium. The emissivity of Sylgard was not found in literature, here we gave to it to be 0.96 of glass. The free convective heat transfer coefficient of 10 W/(m$^2$ K) was applied on all the surfaces exposed to the ambient air as well. In the experiments, an air conditioner was running, and air flow velocity is around 1 m/s, then the convective heat transfer coefficient can be estimated 10 W/(m$^2$ K), see Ref. [28].

An adiabatic boundary condition was fixed to the two side cross-sections of the copper tube, to replicate the thermal insulation as used during the experiments. Based on the flowrate, the velocity magnitude ($2.95 \times 10^{-2}$ m/s) was applied as a boundary condition at the inlet surface of the tube. At the outlet of the tube, the water static pressure was set to be 0 Pa, as is consistent with a “return to tank” line. No-slip boundary conditions were applied on the wet walls to simulate the frictional boundary films present in real heat exchangers.

There were a few interfaces having set up between two different computational domains, such as the interface between the air body in CCPC cavities and CCPC wall, the interface between the air body and PV cell surfaces, the interface between one PV cell surface and one surface of the Sylgard layer and the interface between one surface of the Sylgard layer and the top surface of the tube.

**Table 1**
Thermal, optical, and radiative property constants of materials in CCPC module at 25 °C.

| Property constant | Water | Air | Sylgard | PV cell | CCPC | Tube |
|---|---|---|---|---|---|---|
| Density, kg/m$^3$ | 997.0 | 1.185 | 1030 | 2330 | 840 | 8933 |
| Dynamic viscosity, Pa.s | 8.899e-4 | 1.831e-5 | – | – | – | – |
| Specific capacity, J/(kg K) | 4181.7 | 1004.4 | 1100 | 712 | 903 | 385 |
| Thermal conductivity, W/(m K) | 0.069 | 2.61e-2 | 0.27 | 148 | 0.19 | 401 |
| Refractive index | – | 1.0 | 1.42 | 4.0 | 1.373 | – |
| Absorption coefficient, 1/m | – | 1.0e-2 | 2.0 | 7e+4 | 307 | – |
| Scattering coefficient, 1/m | – | 0.0 | 0.0 | 0.0 | 0.0 | – |
| Emissivity | – | – | 0.06 | – | 0.96 | – |
| Coefficient of Thermal expansion, 1/K | – | 3.356e-3 | – | – | – | – |

The multiphysics simulation above was based on a finite volume method. The radiative heat transfer for the air bodies, CCPCs, PV cells and Sylgard layer was solved using the Monte Carlo method. In doing so a set of meshes, with 610,403 nodes and 1,747,568 elements at 0.5 mm element size and 0.05 mm minimum edge length respectively, were generated using the Meshing module of ANSYS [28]. This used hexahedrons for the heat exchanger tube, tetrahedrons for the air bodies, CCPCs and Sylgard layer, wedges for the fluid domains and pyramids for the air bodies and CCPCs. Also, a 10-layer boundary layer mesh was patched on the tube wet walls to identify the fine flow structure near the walls. The mean element quality, which is based on the ratio of the volume to the sum of the square of the edge lengths for the square root of the cube of the sum of the square of the edge lengths for 3D elements, was calculated to be 0.7295 with a standard deviation 0.1997. Usually, a value of 1 indicates a perfect cube or square element while a value of 0 indicates that the element has a zero or negative volume. Here the obtained 0.7295 mean element quality suggested that the mesh generated in a good quality and the result obtained from ANSYS were a close representative of a realistic system. A part of the mesh generated from these procedures is shown in Fig. 15.

## 4. Results & discussion

### 4.1. Electrical performance

For each set of readings at a given light intensity and inclination angle, IV measurements were taken for both the non-concentrating and the concentrating module. The performance of the CPV module was compared with that of the non-concentrating module for each desired inclination angle. Fig. 16 shows a set of I-V curves for both devices with and without the optical concentrator. As expected, a correlation was seen regarding how the electrical output dropped with an increasing incident angle. The short circuit current remained stable at 400 mA for angles of incidence of 0, 10 and 20 but dropped as the half acceptance angle of 30° was approached. The maximum power output at the “normal incidence” condition for the prototype with concentrators and no water flow was found to be 78.4 mW. The fill factor was recorded to be 72%, which was slightly lower compared to that of the bare solar cell recorded to be 80%, this is primarily an impact of the non-uniformity of the illumination on the solar cell.

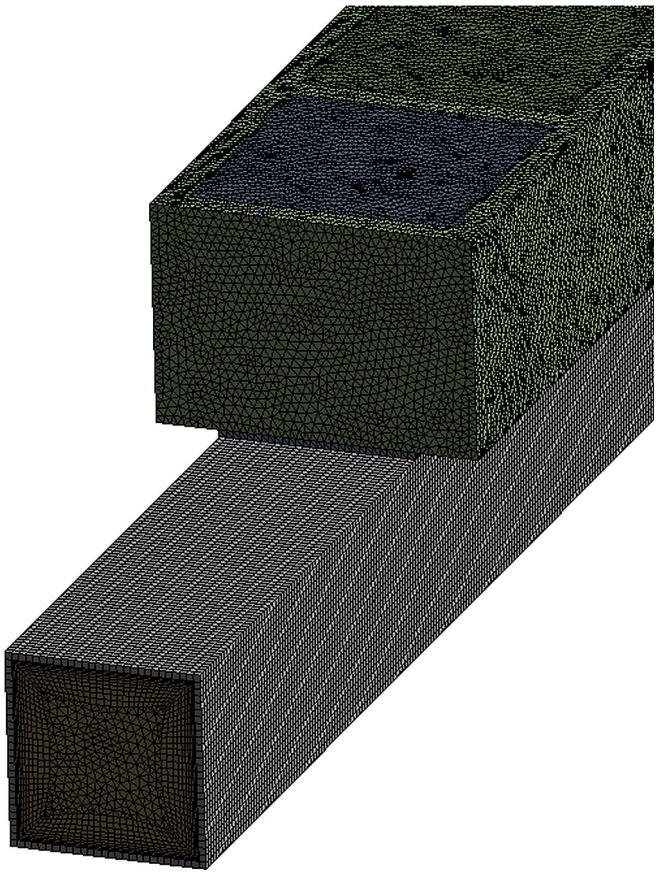

**Fig. 15.** Mesh generated in the computational domain.

### 4.2. Optical performance

The optical efficiency can be defined as the ratio of solar radiation received by the absorber to the radiation incident on the input aperture. The optical efficiency accounts for all possible reflection and transmission losses on the aperture cover. The impact of the sun position on the optical performance was evaluated from the obtained experimental data, while varying the tilt (altitude) and the rotation angle (azimuth) using the setup described earlier and as shown in Fig. 17. Using the parameters obtained via electrical characterisation of the system, the optical efficiency was computed using Eq. (1) as shown below, where Isc refers to the short circuit current and CG is the geometric concentration ratio 3.6 × .

$$Optical\ \ Efficiency = \frac{I_{SC}^{with\ \ concentrator}}{I_{SC}^{without\ \ concentrator}} * \frac{1}{C_G} \tag{1}$$

The maximum optical efficiency of the system was found to be 67% under normal incidence. The optical efficiency remained constant within the angular acceptance range of the concentrator and then as expected from theory was found to drop significantly thereafter as shown in Fig. 18. Experimental analysis of the data obtained showed an increase in power of 141% (power ratio 2.41) compared to the analogous non-concentrating counterpart as shown in Fig. 19. The reflective losses from the rough parabolic surface further reduces the overall optical efficiency of the system, and hence highlights an area of prototype performance improvement with a different manufacturing procedure.

Using the Matlab curve fitting tool the optical efficiency obtained during the experiment was converted into a function of azimuth (a) and altitude angle using Eq. (2) shown below. A fifth-degree polynomial was obtained with an $R^2 = 0.9844$. Using this equation, the optical efficiency for any geographic location can hence be evaluated for any given time and day of the year. Using the geographic location data, the optimum tilt can be estimated. Using this information, the incoming solar radiation and altitude and azimuth angles for any given day and time of the year. Using Eq. (2) the optical efficiency can be calculated and the expected electrical output from the device estimated.

$$\begin{aligned} Eff(a,h) = {} & p00 + p10{*}a + p01{*}h + p20{*}a\hat{2} + p11{*}a{*}h \\ & + p02{*}h\hat{2} + p30{*}a\hat{3} + p21{*}a\hat{2}{*}h + p12{*}a{*}h\hat{2} \\ & + p03{*}h\hat{3} + p40{*}a\hat{4} + p31{*}a\hat{3}{*}h + p22{*}a\hat{2}{*}h\hat{2} \\ & + p13{*}a{*}h\hat{3} + p04{*}h\hat{4} + p50{*}a\hat{5} + p41{*}a\hat{4}{*}h \\ & + p32{*}a\hat{3}{*}h\hat{2} + p23{*}a\hat{2}{*}h\hat{3} + p14{*}a{*}h\hat{4} \\ & + p05{*}h\hat{5} \end{aligned} \tag{2}$$

Using the above-mentioned methodology, the monthly average

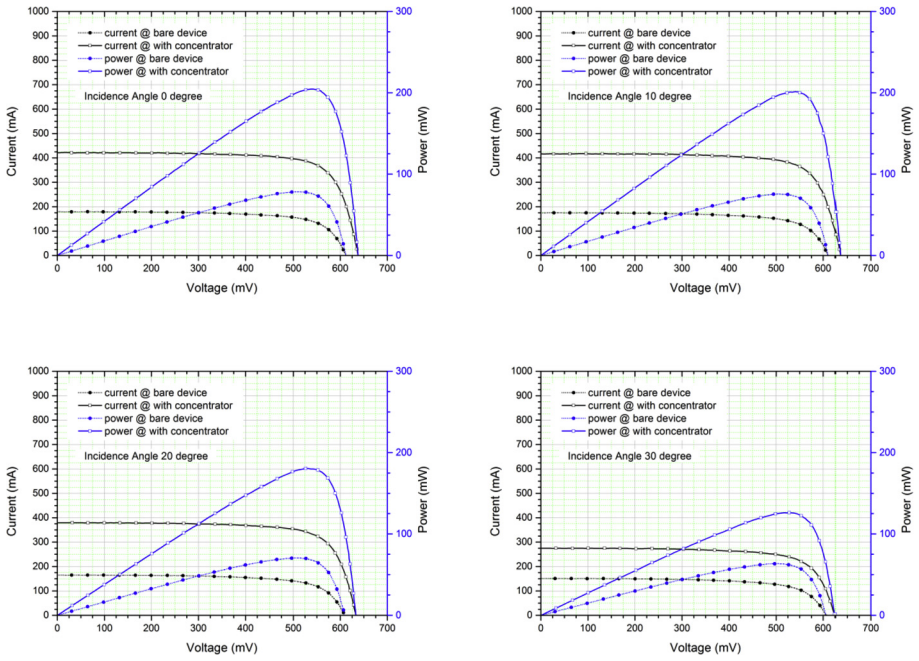


**Fig. 16.** IV-characteristics and power curve of the prototype non-concentrating (bare) module and the concentrator module with 1000 W/m2 radiation intensity incident at 0°, 10°, 20° and 30°.

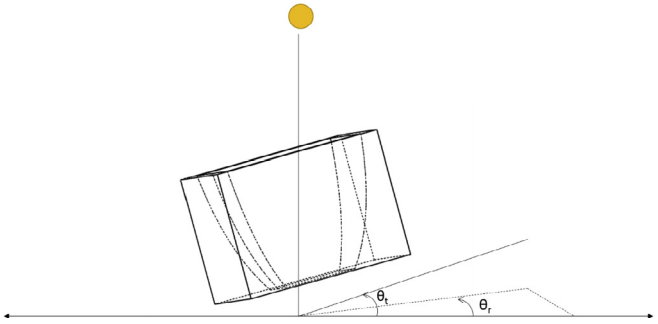


**Fig. 17.** Tilting and rotating the CCPC device.

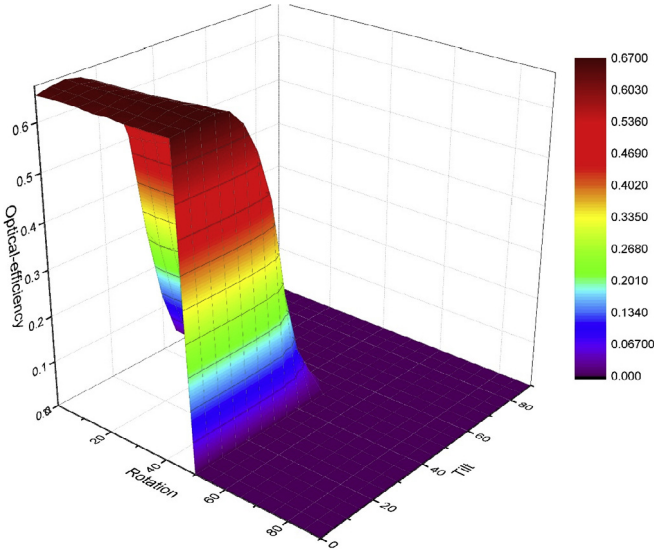


**Fig. 18.** Variation of the optical efficiency with the changing tilt and rotation.

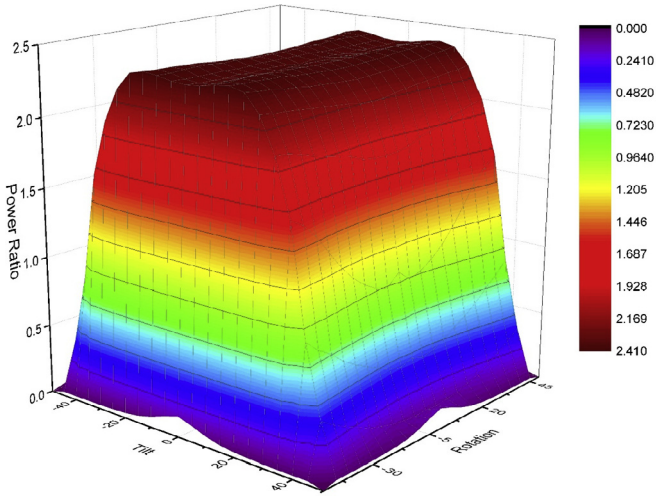


**Fig. 19.** Power ratio of the system.

solar insolation and the expected power output per m2 of the solar cell materials used for six different cities namely Madrid, London, Delhi, Vancouver, Ottawa and Riyad has been forecasted in Fig. 20.

The Meteonorm weather data was used to develop a simple TRNSYS model to evaluate the incident solar radiation and the hourly zenith and azimuth angles on the most optimum tilt plane for a given location as shown in Fig. 20(a). The optical efficiency of the CPV/T system was evaluated using Eq. (2), which was then translated to the estimation of electricity generation per $m^2$ of the photovoltaic material. These values were integrated daily to estimate the monthly performance as shown in Fig. 20(b). The system performs with an average electrical efficiency ranging between 10 and 16% at different locations. For example, in the case of London which receives an annual solar radiation of 1300 kWh/$m^2$ the system is expected to generate 210 kWh/$m^2$. This may reduce further to include losses due to temperature, reflectance/glazing losses,

and electrical losses in cabling and inverter by up to 36% leading to an annual power output of 134 kWh/m$^2$.

### 4.3. Thermal performance

Two cases were studied using this model. The first case was calculating assuming no water flow, i.e., the copper tube is filled with air, and hence this case corresponds to an experimental scenario where there is no water cooling effect. In this case, the water was replaced with a body of air which was subject to the same boundary conditions as the five air bodies in the CCPC cavities. The initial temperature of the computational domain was assigned with the experimentally measured temperature of 34 °C, but for the air bodies in the CCPC cavities, the initial temperature was 25.3 °C as defined by the average ambient temperature recorded during the experiments. The study was performed using 10-min interval under a constant irradiance of 1000 W/m$^2$. The predicted numerical results were found to be within 5% of that obtained during the experiment – further confirming the efficacy of the built ANSYS model. In the second case, is the model assumed water to be

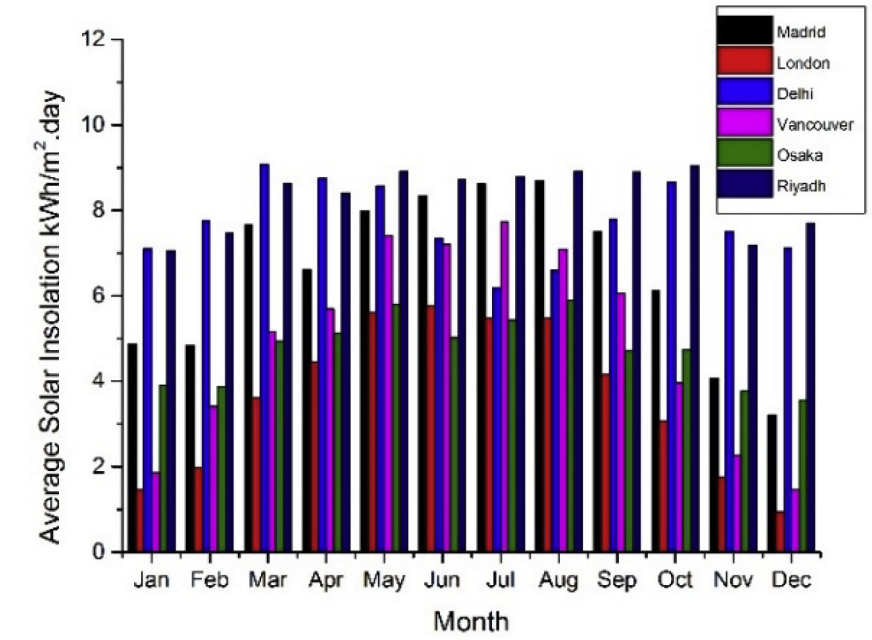


(a)

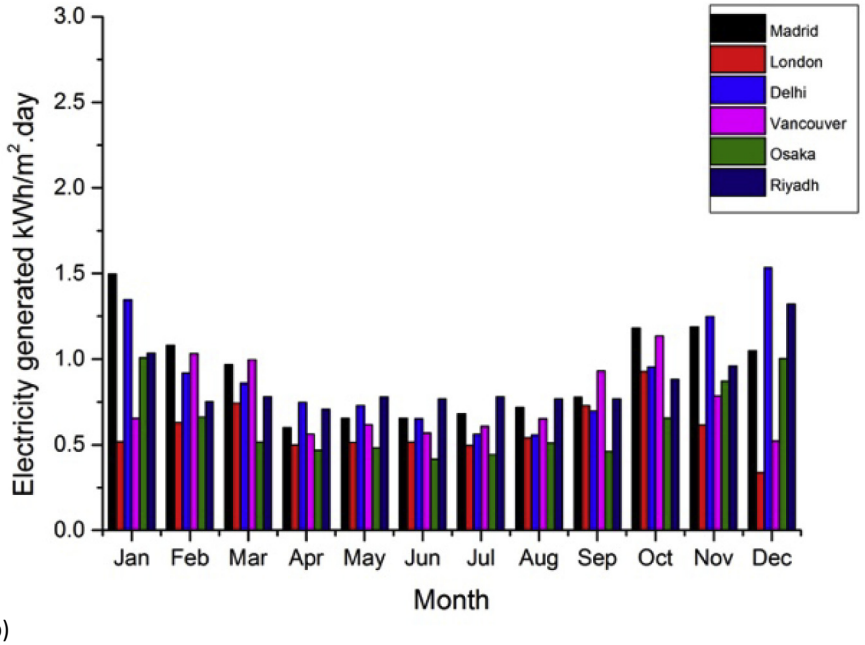


(b)

**Fig. 20.** (a) Average solar insolation at different sites (b) Average electricity production per unit silicon solar cell area.

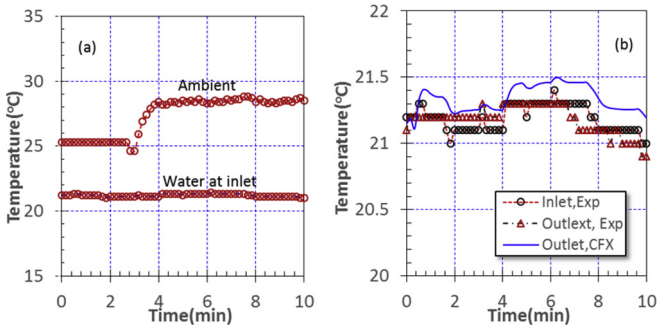


**Fig. 21.** Monitored ambient temperature and water temperature at the tube inlet, and were input into CFX as time-dependent boundary conditions (a) and predicted water temperature in the second case (b).

flowing through the copper tube to cool the PV cells. Here, the water temperature at the tube inlet was used as is shown in Fig. 21(a) and applied in the simulation. The initial temperature of the tube and water was 21.2 °C, while the initial temperature of PV cells is 23.5 °C, the CCPCs and Sylgard layer were subject to 34 °C initial temperature, while the air bodies were in 25.3 °C initial temperature. The predicted water temperature at the tube outlet is presented and compared with the measurement in Fig. 21(b). The predicted temperature across the tube is 0.15 °C in comparison with the temperature difference of 0.1 °C in the experiment. This suggests that the 0.3lit/min water flow rate is so high that the water temperature remains nearly unchanged when it exits tube outlet, even under the LCPV increased irradiance flux. The mean and instantaneous cell and water temperature contours during the 10min duration, for the both cases (with and without water cooling effect) are illustrated in Fig. 22. The mean cell temperature was calculated as the arithmetic mean of all the cell temperatures. In the first case, the predicted mean cell temperature rises linearly with time. In the second case-with water cooling effect, however, the cell temperature is shown to be constant.

In the first case, the tube is full of air, and as such all the cells exhibit approximately the same temperature. The air in the middle of the tube was shown to be at a higher temperature than the air the tube ends. In comparison, for the second case the cell and water temperatures showed a linear correlation along the length of the exchanger tube. The PV cells were modelled as a series heat source along the flow path. In general, the temperature of the cells was found to be higher than the temperature of the water underneath due to the thermal resistances between the cell and the water. It was shown that with a water flow rate of 0.3lit/min and a 21.2 °C inlet temperature, the cell temperature can be effectively cooled to 18 °C within 10 min.

### 4.4. System losses and improvements

In the present study, we have evaluated a hybrid concept for a low concentrator photovoltaic system. The optical efficiency of the system was found to be lower by ~23% than that predicted by the ray trace simulations, due to the rough finishing obtained on the 3D printed concentrator. An alternative method is to make use of the reflective films on a curved parabolic surface. However, our experience shows that high humidity present within the system can cause the peeling of the reflective film and make system failure more likely. Improving the manufacturing of the concentrator, such as by using injection moulding and evaporative coating would improve the overall performance. The second key factor that affected the system performance was the solar cell temperature. When mounted on a copper tube with no fluid running through the system, the solar cell temperature was found to rise due to the thermal resistances of the adhesive. Using a cooling fluid to maintain the solar cell temperature can be beneficial in improving the electricity output through the system whilst simultaneously providing a source of low temperature heat. Controlling the flow-rate of the fluid based on the incoming solar irradiance can prove to be an effective method for the overall improvement of the device. Although the achieved system performance was lower than expected from the design calculations due to the optical losses inherent to our available manufacture procedure, the design presented here highlights the advantages and co-generation benefits that can be achieved using an integrated PV-T co-generation system.

## 5. Conclusions

In this work a Hybrid LCPV/T prototype system was presented. The system was found to have significant improvement as compared with its predecessors. Optical ray tracing was carried to evaluate the concentration of sunlight on the solar cell under different angles of incidence. Fabrication of the optical concentrator was carried out using 3D printing in combination with thermal evaporation techniques for the reflective coating. The bonding of the solar cells to a conductive heat exchanger element was carried out using an oven cured a thermal adhesive between the surfaces. LGBC solar cells with an efficiency of 18% was incorporated in this design under a concentration of 3.6 × . A wide range of illumination intensities and angular positions along both the directions were experimentally achieved using bespoke designed experimental apparatus which gave a better understanding of the variation in the efficiencies with the changing sun position over the whole year. An equation was developed to predict the optical efficiency for any given location as a function of the altitude and the azimuth angles. It was found that the performance of the system was closely

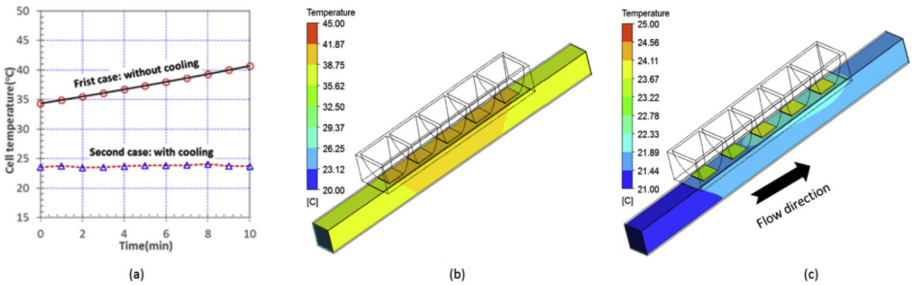


**Fig. 22.** (a) Predicted mean cell temperature as a function of time (b) Temperature plot of the system at 10min without water cooling (c) with water cooling.

dependant on the chosen solar cell technology, the bonding between the solar cell and the heat exchanger and the flowrate of the water through the tube. The heat exchanger considerably reduced the temperature of the solar cell with the increase in the electrical output of the solar cell be experimentally measure and discussed. Changing the flowrate according to the intensity of the incoming radiation was highlighted through this work as a vital optimisation parameter the overall system output and for LCPV-T systems in general. A scale up device based on this concept will be developed to further validate the concept.

**Acknowledgements**

The authors gratefully acknowledge the EPSRC Solar Challenge project SUNTRAP (EP/K022156/1).

## Appendix. The governing equations of optics, heat transfer and fluid flow

### 1 Radiation Transport in Medium

The sunlight is electromagnetic wave with a spectrum and can travel in any kinds of medium and be described by the Maxwell's equations. A CCPC with PV cell can absorb, emit and scatter the sunlight during its propagation. For a plane-parallel medium, the monochromatic radiation intensity of a sunlight beam obeys the following equation along its travel path $s$ [25],

$$\frac{1}{\lambda_\nu(s)}\frac{dI_\nu(\mathrm{r},s)}{ds}+I_{\nu b}(\mathrm{r},s)=S_\nu(s) \tag{A1a}$$

where

$$S_\nu(s)=(1-\omega_\nu)I_{\nu b}(T)+\frac{1}{4\pi}\omega_\nu\int_{4\pi}dI_\nu(\mathrm{r},s')\Phi(\mathrm{s}\cdot s')d\Omega' \tag{A1b}$$

$$\lambda_\nu(s)=\alpha_\nu(s)+\gamma_\nu(s) \tag{A1c}$$

$$\omega_\nu=\frac{\gamma_\nu(s)}{\lambda_\nu(s)} \tag{A1d}$$

$$I_{\nu b}(T)=\frac{2\,m\nu^3}{c^2\left[\exp\left(\frac{m\nu}{\kappa T}\right)-1\right]} \tag{A1e}$$

Here $S_\nu(s)$ is the spectral source function, $\lambda_\nu(s)$ is the spectral extinction coefficient, $\alpha_\nu$ is the absorption coefficient of medium, $\gamma_\nu$ is the scattering coefficient of medium, $\omega_\nu(s)$ is the spectral diffuse reflectivity that is a ratio of the scattering coefficient to the extinction coefficient, $m$ and $\kappa$ are the Planck and Boltzmann constants respectively, $c$ is the speed of sunlight in the medium, $\nu$ is the frequency, $T$ is the absolute temperature, r is the position vector, s is the direction vector, $s$ is the ray path length, $I_{\nu b}(T)$ is the blackbody emission intensity, $I_\nu(\mathrm{r},s)$ is the spectral radiation intensity, $\Omega$ is the solid angle, and $\Phi$ is the scattering phase function.

In simulations in this paper, we assume the medium to be grey and homogenous without any scattering reflection. Thus, the radiative properties of the medium are independent of frequency or wavelength, path length and $\gamma_\nu=\omega_\nu=0$. Eq. (A1a) is integrated over all frequencies, yielding

$$\frac{1}{\kappa}\frac{dI(\mathrm{r},s)}{ds}+I(\mathrm{r},s)=I_b(T) \tag{A2a}$$

with

$$I(\mathrm{r},s)=\int_{\nu=0}^{\infty}I_\nu(\mathrm{r},s)d\nu \tag{A2b}$$

$$\int_{\nu=0}^{\infty}I_{\nu b}(T)d\nu=I_b(T)=\frac{n^2\sigma T^4}{\pi} \tag{A2c}$$

where $\alpha$ is the average absorption coefficient of the medium, $I_b(T)$ is the total blackbody radiation intensity, $\sigma$ is the Stefan-Boltzmann constant, and $n$ is the refractive index of the medium assumed to be independent of frequency. The solar radiation transport behaviour through all the media of the CCPC with solar cell shown in Fig. 14 is obtained by solving Eq. (A2a) with the Monte Carlo method.

### 2 Radiation Transport on Interface

When a beam of sunlight travels through multiple media, it experiences the interfaces between any two media. On the interfaces the sunlight may be reflected and refracted. Considering a beam of sunlight is incident upon the interface between medium 1 and medium 2 as shown Fig. A1. As a result, one beam is reflected bottom to medium 1 with an angle $\theta_1$, and is refracted into medium 2 with an angle $\theta_2$. The two comments of polarization of electrical field of the beam reflected are determined by Fresnel's reflection equations written as [28].

$$\begin{cases}\dfrac{E_{r,\perp}}{E_{i,\perp}}=-\dfrac{\sin(\theta_1-\theta_2)}{\sin(\theta_1+\theta_2)}\\[2ex]\dfrac{E_{r,\parallel}}{E_{i,\parallel}}=\dfrac{\tan(\theta_1-\theta_2)}{\tan(\theta_1+\theta_2)}\end{cases} \tag{A3}$$

where $E_{i,\perp}$ and $E_{i,\parallel}$ denote the two components of the incident beam, one is perpendicular to and the other is parallel to the plane of incidence, likewise, $E_{r,\perp}$ and $E_{r,\parallel}$ represent those of the reflected beam. The ratio of radiation intensity of the reflected beam over that of the incident beam for the components is defined as

$$\begin{cases}\varsigma_{\nu,\perp}=\left(\dfrac{E_{r,\perp}}{E_{i,\perp}}\right)^2=\dfrac{\sin^2(\theta_1-\theta_2)}{\sin^2(\theta_1+\theta_2)}\\[2ex]\varsigma_{\nu,\parallel}=\left(\dfrac{E_{r,\parallel}}{E_{i,\parallel}}\right)^2=\dfrac{\tan^2(\theta_1-\theta_2)}{\tan^2(\theta_1+\theta_2)}\end{cases} \tag{A4a}$$

where $\varsigma_{\nu,\perp}$ and $\varsigma_{\nu,\parallel}$ are the reflectivity of the two components at frequency $\nu$, respectively. In CFX, however, the radiation is considered to be unpolarised and two components are subject to an equal intensity, thus the reflectivity is the average of $\varsigma_{\nu,\perp}$ and $\varsigma_{\nu,\parallel}$, namely,

$$\varsigma_\nu=\frac{1}{2}\left(\varsigma_{\nu,\perp}+\varsigma_{\nu,\parallel}\right)=\frac{1}{2}\left[\frac{\sin^2(\theta_1-\theta_2)}{\sin^2(\theta_1+\theta_2)}+\frac{\tan^2(\theta_1-\theta_2)}{\tan^2(\theta_1+\theta_2)}\right] \tag{A4b}$$

The ratio of radiation intensity of the refracted beam over that of the incident beam can now be expressed as

$$\varepsilon_\nu=1-\varsigma_\nu \tag{A4c}$$

where $\varepsilon_\nu$ is the emissivity or absorptivity of a medium. We have redeemed the grey model above, so that $\varsigma_\nu$ and $\varepsilon_\nu$ are independent of frequency, and hence denoted by $\varsigma$ and $\varepsilon$ respectively.

The angle of refraction $\theta_2$ is determined by using the Snell's law of refraction as below

$$\frac{\sin\theta_2}{\sin\theta_1} = \frac{n_1}{n_2} \tag{A4d}$$

in which $n_1$ and $n_2$ are the refractive index of media 1 and 2 respectively. Ray trace analysis is performed to track the path of the sunlight beam travelling through the interfaces.

3 Fluid Flow Model.

The density of the air in the CCPC cavities varies from the PV cell surface to the CCPC inlet because of the temperature gradient between them. Consequently, the air will be motion in the cavities by the gravity. This upward air current can convey the heat generated from the solar cell surface to the outside of CCPC, eventually this part of heat is dissipated to the environment. It is shown that the Reynolds number of the CCPC is less than 100 determined based on the maximum air velocity at zero incidence, thus suggesting the filled air flow is laminar. In a stationary reference frame, the instantaneous continuity, momentum and thermal energy equations can be written as [26]:

$$\frac{\partial\rho}{\partial t} + \nabla\cdot(\rho\vec{U}) = 0 \tag{A5a}$$

$$\frac{\partial(\rho\vec{U})}{\partial t} + \nabla\cdot(\rho\vec{U}\otimes\vec{U}) = -\nabla p + \nabla\cdot\tau + \vec{F} \tag{A5b}$$

$$\frac{\partial(\rho e)}{\partial t} + \nabla\cdot(\rho\vec{U}e) = \nabla\cdot(\lambda T) + \tau : \nabla\vec{U} + S_E \tag{A5c}$$

where $\rho$, $\vec{U}$, $p$, $\tau$, $\vec{F}$, $e$, $T$, $\lambda$ and $S_E$ are the density, velocity, pressure, shear stress tensor, body force, internal energy, temperature, heat conductivity and energy source of air, respectively. Here the body force $\vec{F}$ takes into account the buoyancy force, i.e.

$$\vec{F} = \left(\rho - \rho_{ref}\right)\vec{g} \tag{A5d}$$

where $\rho_{ref}$ is the reference density of air at a reference temperature $T_{ref} = 25\,^{\circ}\mathrm{C}$. Since the temperature difference across a CCPC is small, the Boussinesq model is adopted to calculate the density difference, $\rho - \rho_{ref}$, namely

$$\left(\rho - \rho_{ref}\right) = -\rho_{ref}\beta\left(T - T_{ref}\right) \tag{A5e}$$

where $\beta$ is the thermal expansion of air, and defined as

$$\beta = -\frac{1}{\rho}\frac{\partial p}{\partial T}\bigg|_p \tag{A5f}$$

Note that in the Boussinesq model, a constant reference density $\rho_{ref}$ is applied into all terms in the continuity and momentum equations except in the body force $\vec{F}$. In addition, the pressure in the momentum equations excludes the hydrostatic gradient caused by $\rho_{ref}$. The energy source term $S_E$ is considered to be zero.

Since there is no fluid flow inside the solid domains such as the CCPC and tube, sylgard and PV cell layers, the thermal energy equation, Eq. (A5c), is simplified to the following heat transfer equation

$$\frac{\partial(\rho c_p T)}{\partial t} = \nabla\cdot(\lambda\nabla T) + S_E \tag{A6}$$

where $\rho$, $c_p$ and $\lambda$ are the density, specific heat capacity and thermal conductivity of the solids, respectively; the energy source term $S_E$ is still zero.

The above governing equations are solved sequentially in ANSYS 15.0 CFX under a set of appropriate boundary conditions until a solution convergence is reached.

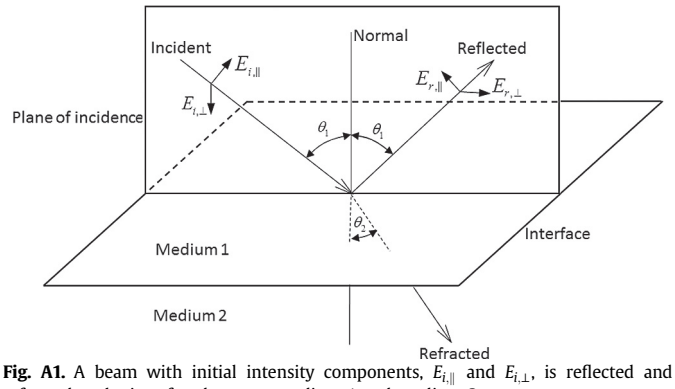


**Fig. A1.** A beam with initial intensity components, $E_{i,\parallel}$ and $E_{i,\perp}$, is reflected and refracted at the interface between medium 1 and medium 2.

## References


[1] Brogren M, Nostell P, Karlsson B. Optical efficiency of a PV–thermal hybrid CPC module for high latitudes. Sol Energy 2001;69(Supplement 6):173–85.

[2] Fraunhofer I. Photovoltaics report Freiburg. Germany: Fraunhofer Institute for Solar Energy Systems, ISE; 2016.

[3] Baig H, Heasman KC, Sarmah N, Mallick TK, Solar cells design for low and medium concentrating photovoltaic systems. Conference solar cells design for low and medium concentrating photovoltaic systems, vol. 1477. AIP Publishing, p. 98–101.

[4] Baig H, Heasman KC, Mallick TK. Non-uniform illumination in concentrating solar cells. Renew Sustain Energy Rev 2012;16(8):5890–909.

[5] Mallick TK, Eames PC, Norton B. Using air flow to alleviate temperature elevation in solar cells within asymmetric compound parabolic concentrators. Sol Energy 2007;81(2):173–84.

[6] Baig Hasan, Sellami Nazmi, Chemisana Daniel, Rosell Joan, Mallick Tapas K. Performance analysis of a dielectric based 3D building integrated concentrating photovoltaic system. Solar Energy 2014;103:525–40.

[7] Ramirez-Iniguez R, Muhammad-Sukki F, Abu-Bakar SR, McMeekin SG, Stewart BG, Sarmah N, et al. Rotationally asymmetric optical concentrators for solar PV and BIPV systems. Conference Rotationally asymmetric optical concentrators for solar PV and BIPV systems. p. 15–17.

[8] Baig H, Sarmah N, Chemisana D, Rosell J, Mallick TK. Enhancing performance of a linear dielectric based concentrating photovoltaic system using a reflective film along the edge. Energy 2014;73(0):177–91.

[9] Rönnelid M, Perers B, Karlsson B. Construction and testing of a large-area CPC-collector and comparison with a flat plate collector. Sol Energy 1996;57(3):177–84.

[10] Goodman NB, Ignatius R, Wharton L, Winston R. Solid-dielectric compound parabolic concentrators: on their use with photovoltaic devices. Appl Optic 1976;15(10):2434–6.

[11] Winston R. Dielectric compound parabolic concentrators. Appl Optic 1976;15(2):291–2.

[12] Winston R. Principles of solar concentrators of a novel design. Sol Energy 1974;16(2):89–95.

[13] Rabl A. Optical and thermal properties of compound parabolic concentrators. Sol Energy 1976;18(6):497–511.

[14] Mallick TK, Eames PC. Electrical performance evaluation of low-concentrating non-imaging photovoltaic concentrator. Prog Photovoltaics Res Appl 2008;16(5):389–98.

[15] Mallick TK, Eames PC, Hyde TJ, Norton B. The design and experimental characterisation of an asymmetric compound parabolic photovoltaic concentrator for building façade integration in the UK. Sol Energy 2004;77(3):319–27.

[16] Mammo ED, Sellami N, Mallick TK. Performance analysis of a reflective 3D crossed compound parabolic concentrating photovoltaic system for building façade integration. Prog Photovoltaics Res Appl 2012:1095–103.

[17] Yousef MS, Abdel Rahman AK, Ookawara S. Performance investigation of low – concentration photovoltaic systems under hot and arid conditions: experimental and numerical results. Energy Convers Manag 2016;128:82–94.

[18] Li G, Pei G, Ji J, Su Y. Outdoor overall performance of a novel air-gap-lens-walled compound parabolic concentrator (ALCPC) incorporated with photovoltaic/thermal system. Appl Energy 2015;144:214–23.

[19] Bahaidarah HM, Tanweer B, Gandhidasan P, Ibrahim N, Rehman S. Experimental and numerical study on non-concentrating and symmetric unglazed compound parabolic photovoltaic concentration systems. Appl Energy 2014;136:527–36.

[20] Abdelhamid M, Widyolar BK, Jiang L, Winston R, Yablonovitch E, Scranton G, et al. Novel double-stage high-concentrated solar hybrid photovoltaic/thermal (PV/T) collector with nonimaging optics and GaAs solar cells reflector. Appl Energy 2016;182:68–79.

[21] Baig H, Sellami N, Bahaidarah H, Mallick TK. Optical analysis of a CPC based CPV/T system for application in the Kingdom of Saudi Arabia. Conference optical analysis of a CPC based CPV/T system for application in the Kingdom of Saudi Arabia, vol. 6. p. 653–657.
[22] http://www.breault.com/software/about-apex.
[23] Heasman AC KC, Roberts S, Brown M, Baistow I, Devenport S, Bruton TM. Development of LGBC solar cells for use at concentration factors up to 100x. In: 4th International conference on solar concentrators (ICSC-4). Spain; 2007.
[24] Baig H, Sarmah N, Heasman KC, Mallick TK. Numerical modelling and experimental validation of a low concentrating photovoltaic system. Sol Energy Mater Sol Cell 2013;113:201–19.
[25] Grena R. An algorithm for the computation of the solar position. Sol Energy 2008;82(5):462–70.
[26] Mouser E. L3G4200D MEMS motion sensor: ultra-stable three-axis digital output gyroscope. 2017.
[27] Baig H, Sellami N, Mallick TK. Performance modeling and testing of a building integrated concentrating photovoltaic (BICPV) system. Sol Energy Mater Sol Cell 2015;134(0):29–44.
[28] Kurazumi Y, Reagals L, Melikov AK. Convective heat transfer coefficients of the human body under forced convection from ceiling. J Ergon 2014;4(1):1–6.